Design of praseodymium-doped chalcogenide micro-disk emitting at 4.7 μm

Giuseppe Palma, Mario Christian Falconi, Florent Starecki, Virginie Nazabal, Julien Ari, Loïc Bodiou, Joël Charrier, Yannick Dumeige, Emeline Baudet, Francesco Prudenzano

Research Article | Vol. 25, No. 6 | 20 Mar 2017 | OPTICS EXPRESS 7014
Optics EXPRESS

Design of praseodymium-doped chalcogenide micro-disk emitting at 4.7 µm

GIUSEPPE PALMA,[1] MARIO CHRISTIAN FALCONI,[1] FLORENT STARECKI,[2] VIRGINIE NAZABAL,[2] JULIEN ARI,[2] LOIC BODIOU,[3] JOEL CHARRIER,[3] YANNICK DUMEIGE,[3] EMELINE BAUDET,[4] AND FRANCESCO PRUDENZANO[1,*]

[1]*Department of Electrical and Information Engineering, Politecnico di Bari, 70125 Bari, Italy*
[2]*Institut des Sciences Chimiques de Rennes, UMR-CNRS 6226, Equipe Verres et Céramiques, Université de Rennes 1, 35042 Rennes, France*
[3]*FOTON-UMR-CNRS 6082, ENSSAT BP80518, F-22305 Lannion Cedex, France*
[4]*Department of Graphic Arts and Photophysics, Faculty of Chemical Technology, University of Pardubice, Studentska 573, 53210 Pardubice, Czech Republic*
[*]*francesco.prudenzano@poliba.it*
https://www.moe-group.it/

Abstract: A compact amplifier based on chalcogenide Pr^{3+}-doped micro-disk coupled to two ridge waveguides is designed and refined by means of a home-made computer code. The gain $G \approx 7.9$ dB is simulated for a Pr^{3+} concentration of 10 000 ppm, input signal power of −30 dBm at the wavelength 4.7 µm and input pump power of 50 mW at the wavelength 1.55 µm. In the laser behavior, i.e. without input signal, the maximum slope efficiency $S = 8.1 \times 10^{-4}$ is obtained for an input pump power of 2 mW. This value is about six times higher than that simulated for an optimized erbium-doped micro-disk.

OCIS codes: (130.2755) Glass waveguides; (140.3410) Laser resonators; (140.3945) Microcavities; (140.4480) Optical amplifiers; (140.4780) Optical resonators; (160.5690) Rare-earth-doped materials.

References and links

1. Y. Dumeige and P. Féron, "Coupled optical microresonators for microwave all-optical generation and processing," Opt. Lett. **40**(14), 3237–3240 (2015).
2. T. Kishi, T. Kumagai, S. Shibuya, F. Prudenzano, T. Yano, and S. Shibata, "Quasi-single mode laser output from a terrace structure added on a Nd3+-doped tellurite-glass microsphere prepared using localized laser heating," Opt. Express **23**(16), 20629–20635 (2015).
3. P. Girault, N. Lorrain, J. Lemaitre, L. Poffo, M. Guendouz, I. Hardy, M. Gadonna, A. Gutierrez, L. Bodiou, and J. Charrier, "Racetrack micro-resonators based on ridge waveguides made of porous silica," Opt. Mater. **50, Part B**, 167–174 (2015).
4. Z. Tian, C. Chen, and D. V. Plant, "Single- and dual-wavelength fiber ring laser using fiber microdisk resonator," IEEE Photon. Technol. Lett. **22**(22), 1644–1646 (2010).
5. Z. Tian, P. Bianucci, and D. V. Plant, "Fiber ring laser using optical fiber microdisk as reflection mirror," IEEE Photon. Technol. Lett. **24**(16), 1396–1398 (2012).
6. S. Calvez, G. Lafleur, A. Larrue, P. F. Calmon, A. Arnoult, G. Almuneau, and O. Gauthier-Lafaye, "Vertically coupled microdisk resonators using AlGaAs/AlOx technology," IEEE Photon. Technol. Lett. **27**(9), 982–985 (2015).
7. A. D'Orazio, M. De Sario, C. Giasi, L. Mescia, V. Petruzzelli, and F. Prudenzano, "Design of planar optic sensors for hydrocarbon detection," Opt. Quantum Electron. **36**(6), 507–526 (2004).
8. M.-L. Anne, J. Keirsse, V. Nazabal, K. Hyodo, S. Inoue, C. Boussard-Pledel, H. Lhermite, J. Charrier, K. Yanakata, O. Loreal, J. Le Person, F. Colas, C. Compère, and B. Bureau, "Chalcogenide glass optical waveguides for infrared biosensing," Sensors **9**(9), 7398–7411 (2009).
9. J.-L. Adam, L. Calvez, J. Trolès, and V. Nazabal, "Chalcogenide glasses for infrared photonics," Int. J. Appl. Glass Sci. **6**(3), 287–294 (2015).
10. A. B. Seddon, Z. Tang, D. Furniss, S. Sujecki, and T. M. Benson, "Progress in rare-earth-doped mid-infrared fiber lasers," Opt. Express **18**(25), 26704–26719 (2010).
11. R. Chahal, F. Starecki, C. Boussard-Plédel, J.-L. Doualan, K. Michel, L. Brilland, A. Braud, P. Camy, B. Bureau, and V. Nazabal, "Fiber evanescent wave spectroscopy based on IR fluorescent chalcogenide fibers," Sens. Actuat. B-Chem. **229**, 209–216 (2016).

#284702 https://doi.org/10.1364/OE.25.007014
Journal © 2017 Received 13 Jan 2017; revised 17 Feb 2017; accepted 17 Feb 2017; published 16 Mar 2017

12. J. Hu, V. Tarasov, A. Agarwal, L. Kimerling, N. Carlie, L. Petit, and K. Richardson, "Fabrication and testing of planar chalcogenide waveguide integrated microfluidic sensor," Opt. Express **15**(5), 2307–2314 (2007).
13. J. Hu, J. D. Musgraves, N. Carlie, B. Zdyrko, I. Luzinov, A. Agarwal, K. Richardson, and L. Kimerling, "Development of chipscale chalcogenide glass based infrared chemical sensors," Proc. SPIE **7945**, 79452C (2011).
14. C. Grillet, S. N. Bian, E. C. Magi, and B. J. Eggleton, "Fiber taper coupling to chalcogenide microsphere modes," Appl. Phys. Lett. **92**(17), 171109 (2008).
15. A. K. Mairaj, C. Riziotis, A. M. Chardon, P. G. R. Smith, D. P. Shepherd, and D. W. Hewak, "Development of channel waveguide lasers in Nd3+-doped chalcogenide (Ga:La:S) glass through photoinduced material modification," Appl. Phys. Lett. **81**(20), 3708–3710 (2002).
16. K. Sasagawa, Z. Yonezawa, R. Iwai, J. Ohta, and M. Nunoshita, "S-band Tm3+-doped tellurite glass microsphere laser via a cascade process," Appl. Phys. Lett. **85**(19), 4325–4327 (2004).
17. J. Wu, S. Jiang, T. Qua, M. Kuwata-Gonokami, and N. Peyghambarian, "2 m lasing from highly thulium doped tellurite glass microsphere," Appl. Phys. Lett. **87**(21), 211118 (2005).
18. F. Starecki, F. Charpentier, J.-L. Doualan, L. Quetel, K. Michel, R. Chahal, J. Trolès, B. Bureau, A. Braud, P. Camy, V. Moizan, and V. Nazabal, "Mid-IR optical sensor for CO2 detection based on fluorescence absorbance of Dy3+:Ga5Ge20Sb10S65 fibers," Sens. Actuat. B-Chem. **207, Part A**(5), 518–525 (2015).
19. A. L. Pelé, A. Braud, J. L. Doualan, F. Starecki, V. Nazabal, R. Chahal, C. Boussard-Plédel, B. Bureau, R. Moncorgé, and P. Camy, "Dy3+ doped GeGaSbS fluorescent fiber at 4.4 m for optical gas sensing: comparison of simulation and experiment," Opt. Mater. **61**, 37–44 (2016).
20. M. C. Falconi, G. Palma, F. Starecki, V. Nazabal, J. Trolès, S. Taccheo, M. Ferrari, and F. Prudenzano, "Design of an efficient pumping scheme for mid-IR Dy3+:Ga5Ge20Sb10S65 PCF fiber laser," IEEE Photon. Technol. Lett. **28**(18), 1984–1987 (2016).
21. M. C. Falconi, G. Palma, F. Starecki, V. Nazabal, J. Trolès, J.-L. Adam, S. Taccheo, M. Ferrari, and F. Prudenzano, "Dysprosium-doped chalcogenide master oscillator power amplifier (MOPA) for mid-IR emission," J. Lightwave Technol. **35**(2), 265–273 (2017).
22. V. Nazabal, F. Starecki, J.-L. Doualan, P. Němec, P. Camy, H. Lhermite, L. Bodiou, M. L. Anne, J. Charrier, and J.-L. Adam, "Luminescence at 2.8 m: Er3+-doped chalcogenide micro-waveguide," Opt. Mater. **58**, 390–397 (2016).
23. Z. Tang, D. Furniss, M. Fay, H. Sakr, L. Sójka, N. Neate, N. Weston, S. Sujecki, T. M. Benson, and A. B. Seddon, "Mid-infrared photoluminescence in small-core fiber of praseodymium-ion doped selenide-based chalcogenide glass," Opt. Mater. Express **5**(4), 870–886 (2015).
24. H. Lin, L. Li, Y. Zou, S. Danto, J. D. Musgraves, K. Richardson, S. Kozacik, M. Murakowski, D. Prather, P. T. Lin, V. Singh, A. Agarwal, L. C. Kimerling, and J. Hu, "Demonstration of high-Q mid-infrared chalcogenide glass-on-silicon resonators," Opt. Lett. **38**(9), 1470–1472 (2013).
25. L. Mescia, P. Bia, O. Losito, and F. Prudenzano, "Design of mid-IR Er3+-doped microsphere laser," IEEE Photon. J. **5**(4), 1501308 (2013).
26. F. Prudenzano, L. Mescia, L. Allegretti, V. Moizan, V. Nazabal, and F. Smektala, "Theoretical study of cascade laser in erbium-doped chalcogenide glass fibers," Opt. Mater. **33**(2), 241–245 (2010).
27. G. Palma, C. Falconi, V. Nazabal, T. Yano, T. Kishi, T. Kumagai, M. Ferrari, and F. Prudenzano, "Modeling of whispering gallery modes for rare earth spectroscopic characterization," IEEE Photon. Technol. Lett. **27**(17), 1861–1863 (2015).
28. G. Palma, M. C. Falconi, F. Starecki, V. Nazabal, T. Yano, T. Kishi, T. Kumagai, and F. Prudenzano, "Novel double step approach for optical sensing via microsphere WGM resonance," Opt. Express **24**(23), 26956–26971 (2016).
29. S. Sergent and F. Semond, "(Al,Ga)N Microdisk Cavities," in "Handbook of Optical Microcavities," A. H. W. Choi, ed. (Pan Stanford Publishing Pte. Ltd., 2014), Chap. 4.
30. R. R. A. Syms and J. R. Cozens, *Optical Guided Waves and Devices* (McGraw-Hill, 1992).
31. B. E. Little, S. T. Chu, H. A. Haus, J. Foresi, and J. P. Laine, "Microring resonator channel dropping filters," J. Lightwave Technol. **15**(6), 998–1005 (1997).
32. B. E. Little, J. P. Laine, and H. A. Haus, "Analytic theory of coupling from tapered fibers and half-blocks into microsphere resonators," J. Lightwave Technol. **17**(4), 704–715 (1999).
33. M. Borselli, T. J. Johnson, and O. Painter, "Beyond the Rayleigh scattering limit in high-Q silicon microdisks: theory and experiment," Opt. Express **13**(5), 1515–1530 (2005).
34. C. A. Balanis, *Advanced Engineering Electromagnetics* (Wiley, 1989), 1st ed.
35. F. Al Tal, C. Dimas, J. Hu, A. Agarwal, and L. C. Kimerling, "Simulation of an erbium-doped chalcogenide micro-disk mid-infrared laser source," Opt. Express **19**(13), 11951–11962 (2011).
36. P. Němec, M. Olivier, E. Baudet, A. Kalendová, P. Benda, and V. Nazabal, "Optical properties of (GeSe2)100-x(Sb2Se3)x glasses in near- and middle-infrared spectral regions," Mater. Res. Bull. **51**, 176–179 (2014).

1. Introduction

Whispering gallery mode resonators are characterized by low reflection losses and very small sizes. These peculiarities allow extremely small mode volumes, high power densities and high-quality factors Q. Their compactness and manufacturing cost are very attractive items for actual

photonic applications.

Microspheres and micro-disks have been largely investigated as key elements in a number of optical sensing set-ups. They exhibit, in many respects, strong points and drawbacks. Micro-disks allow potentially higher integration degree, within complex optical circuits, than microspheres [1, 2], mechanical stability and low-cost fabrication. A drawback is the lower quality factor in comparison with microspheres. This is due to the higher optical losses caused by the technological fabrication process [3]. A common technique for fabricating micro-disks is the conventional photolithography and reactive ion etching process [3]. An alternative technique is based on optical fiber tapering, cleaving and splicing [4]. Micro-disks made through these fabrication procedures exhibit good quality factors, close to $Q = 8 \times 10^6$ [5]. Moreover, a micro-disk resonator vertically coupled to a buried oxide access waveguide, using AlGaAs/AlOx technology, was demonstrated in [6]. The sample, resonating at the wavelength $\lambda = 1.6\,\mu m$, exhibited quality factors up to $Q = 8.5 \times 10^3$.

Mid-infrared wavelength range promises a number of applications in different fields such as spectroscopy and optical sensing. Novel sensing set-ups can be designed to detect the vibrational transitions exhibited by many organic species and biomolecules [7, 8]. Rare earth doped micro-disks can be employed in order to fabricate active sensors, dramatically increasing the light interaction with chemical or biological species lying in the medium surrounding their surface. The optimization of these optical structures in the medium infrared wavelength range is welcome in order to obtain strong resonant wavelength shift or strong absorption as main effects to be exploited for sensing operation.

Chalcogenide glasses (ChG) are characterized by a wide transmissivity, in both near- and mid-infrared wavelength ranges. In addition, they have relatively good mechanical strength, chemical durability in water and atmosphere [9, 10], high linear and nonlinear refractive index, photosensitivity, high quantum efficiency and large radiative decay rates [11–14]. Moreover, chalcogenide glasses can be host materials for rare earths, providing efficient emission especially in the mid-infrared because of their low phonon energy [9]. As an example, lasing in chalcogenide glasses doped with neodymium and thulium is reported in [15–17]; dysprosium luminescence is exploited for the fabrication of an active chalcogenide CO_2 sensor at $\lambda = 4.35\,\mu m$ [18–21]; erbium luminescence in micro-waveguide at $\lambda = 2.8\,\mu m$ is illustrated in [22]; mid-infrared photoluminescence of praseodymium-doped chalcogenide fibers is reported in [23]. The feasibility of ChG-on-silicon mid-IR micro-resonators with an intrinsic quality factor $Q = 2 \times 10^5$ at $\lambda = 5.2\,\mu m$ is demonstrated in [24].

In this paper, a home-made code is developed and exploited in order to design a chalcogenide Pr^{3+}-doped resonant micro-disk. It is coupled to two ridge waveguides, the former guiding the pump beam and the latter the signal to be amplified/generated. To the best of our knowledge, for the first time a Pr^{3+}-doped micro-disk amplifying/lasing at $\lambda \approx 4700\,nm$ is optimized and its feasibility is investigated.

2. Theory

The model and the design procedures are divided in three main sections:

- passive structure model, in order to obtain the electromagnetic field profile of both micro-resonator and optical waveguides, by neglecting the rare earth; this section is subdivided in two subsections: a) passive structure coarse model (design) and b) passive structure refined model (design);
- optical coupling model, based on the coupled mode theory in order to simulate the coupling between the resonator and the waveguides;
- active behavior model, based on the rate equations for the rare-earth ions population

Optics EXPRESS

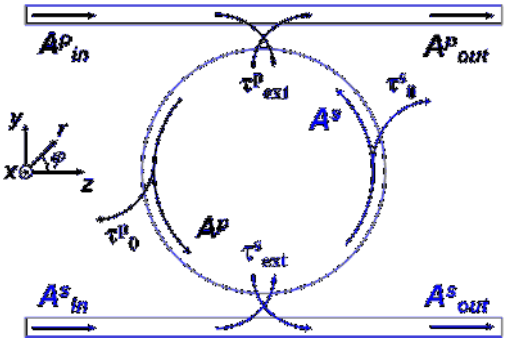

Fig. 1. Micro-disk coupled to two ridge waveguides, one for the pump P and the other for the signal S. A_{in}, A_{out} and A are the amplitudes of electromagnetic field at the input and output waveguide sections and inside the micro-disk, respectively. τ_{ext} and τ_0 are the coupling and intrinsic lifetimes, respectively.

densities in order to simulate the optical gain/lasing. This model scheme is similar to that used in [25–28].

This approach can be followed, more in general, for the simulation of any active WGM micro-resonator.

2.1. Passive structure model

The Pr^{3+}-doped micro-disk coupled to two ridge waveguides, one for the signal and the other one for the pump, is sketched in Fig. 1. $A^{\text{P,S}}_{\text{in}}$, $A^{\text{P,S}}_{\text{out}}$ and $A^{\text{P,S}}$ are the amplitudes of electromagnetic field at the input and output waveguide sections and inside the micro-disk, respectively; the superscripts P and S indicate the pump and signal, respectively; τ_{ext} and τ_0 are the coupling and intrinsic lifetimes, respectively. These parameters will be defined in the following.

A preliminary design, i.e. the passive structure coarse design a) of the micro-disk is carried out by considering the whispering gallery mode analytic expression, i.e. their closed form [29]. The implemented computer code is very quick since the solutions of the closed/analytical formulation are found. In fact, the micro-disk is considered as a 1D, slab waveguide, in order to calculate the mode effective refractive index n_{eff}. The structure is constituted by three layers: air, micro-disk core, buffer. Air and buffer layers are considered semi-infinite. The micro-disk thickness is $h_{\mu\text{disk}}$. The micro-disk core has a refractive index higher than that of the other layers, so the total internal reflection occurs at each interface.

With the reference frame reported in Fig. 1 and the aforementioned approximation, light propagates in the equivalent waveguide along z with an exponential variation $\exp(-\gamma z)$. The electromagnetic analysis of the slab waveguide is developed by finding the solutions of the Helmholtz equation in Cartesian coordinates.

By considering the transverse electric (TE) modes, the electric field components along x and z become negligible compared to y component. The Helmholtz equation can be simplified as follows [29]:

$$\frac{\partial^2 E_{y,i}(x)}{\partial x^2} = (k_i^2 - \gamma^2) E_{y,i}(x) \tag{1}$$

where $E_{y,i}$ is the y component of the electric field $\mathbf{E}$; $k_i = \omega\sqrt{\mu_i \varepsilon_i}$ is the wave vector in the layer i; $\gamma = k n_{\text{eff}}$ is the propagation constant along z; n_{eff} is the effective refractive index; $k = \omega\sqrt{\mu_0 \varepsilon_0}$ is the wave vector in vacuum; μ_0 and ε_0 are the vacuum permeability and permittivity, respectively.

By imposing the boundary conditions, the characteristic equation is obtained [30]:

$$\tan(\nu h_{\mu\text{disk}}) = \frac{\nu(\eta + \chi)}{\nu^2 - \eta\chi} \tag{2}$$

where:

$$\nu = \sqrt{n_{\mu\text{disk}}^2 k^2 - \gamma^2},\ \eta = \sqrt{\gamma^2 - n_{\text{buffer}}^2 k^2},\ \chi = \sqrt{\gamma^2 - n_{\text{air}}^2 k^2} \tag{3}$$

$h_{\mu\text{disk}}$ is the micro-disk thickness, $n_{\mu\text{disk}}$, n_{buffer} and n_{air} are the refractive indices of micro-disk core, buffer and air, respectively. The effective refractive index n_{eff} of the structure is obtained by Eq. (1). Each solution is labeled with the parameter p related to the modal order. The parameter p represents the number of field maxima in the transversal direction x. This method applied to the slab waveguide is generally known as EIM (effective index method) in x direction. The effective refractive index n_{eff} is employed in the 2D analysis over the equatorial plane y-z involving the cylindrical Bessel equation [29]. More precisely, the 2D characteristic equation of the micro-disk is written. The separation of the cylindrical variables r, φ (see Fig. 1) in Helmholtz equation is exploited to obtain the radial component of the electric field outside the micro-disk ($r > R_{\mu\text{disk}}$), as reported in Eq. (4) [29].

$$E_r(r,\varphi) = N\mathrm{J}_m\left(\frac{2\pi}{\lambda_r} n_{\text{eff}} r\right) \exp\left[\frac{2\pi}{\lambda_r}\sqrt{n_{\text{eff}}^2 - n_{\text{air}}^2 (r-a)}\right] \exp(jm\varphi) \tag{4}$$

where N is a constant obtained by imposing boundary conditions; J_m is the Bessel function of first kind of order m; λ_r is the resonant wavelength; $R_{\mu\text{disk}}$ is the micro-disk radius; m is the azimuthal parameter, i.e. the number of electromagnetic field maxima in the azimuthal direction.

The boundary condition $E_r(r,\varphi) = 0$ is imposed for $r > R_{\mu\text{disk}}$. Therefore, Eq. (5) is written:

$$E_r(r,\varphi) = 0 \Rightarrow \mathrm{J}_m\left(\frac{2\pi}{\lambda_r} n_{\text{eff}} R_{\mu\text{disk}}\right) = 0 \tag{5}$$

By solving Eq. (5), the micro-disk radius $R_{\mu\text{disk}}$ and the azimuthal parameter m are calculated for each resonant wavelength λ_r. Therefore, each $\mathrm{WGM_{m,n,p}}$ in the micro-disk is characterized by the three parameter m, n and p. The radial parameter n is the number of field maxima along the radial direction. By employing the aforementioned model, the electromagnetic design of the passive structure is coarsely performed.

The passive structure refined design b) is performed via a full vectorial finite element method solver (FEM). It is used to accurately simulate the electromagnetic field profile for waveguides and micro-disk at the signal and pump wavelengths. The waveguides are designed to operate in single mode regime. The FEM recovered electromagnetic field profiles of the WGMs and of the waveguide modes are used in the rate equations described in the following section on optical coupling.

2.2. Optical coupling model

The optical coupling between the micro-disk and the waveguides is evaluated by using the coupled mode theory [31]. Some assumptions are made in the developed model: i) weak coupling, ii) slowly varying amplitude approximation.

The micro-disk is considered as a lumped system. The amplitude of the electromagnetic field in the micro-disk is $A^{\mathrm{P/S}}$, where the superscripts P and S indicate the pump and signal, respectively. The time evolution of $A^{\mathrm{P/S}}$ in the micro-disk is expressed as follows [32]:

$$\frac{\mathrm{d}A^{\mathrm{P/S}}}{\mathrm{d}t} = \left(-\frac{1}{\tau_0^{\mathrm{P/S}}} - \frac{2}{\tau_{\text{ext}}^{\mathrm{P/S}}} + g^{\mathrm{P/S}} + j\Delta\omega\right) A^{\mathrm{P/S}} - j\sqrt{\frac{2}{\tau_{\text{ext}}^{\mathrm{P/S}} T_{\text{rtt}}}} A_{\text{in}}^{\mathrm{P/S}} \tag{6}$$

$\Delta\omega = \omega_w - \omega_{\mu disk}$ is the frequency detuning, i.e. the difference between input waveguide frequency ω_w and micro-disk resonant frequency $\omega_{\mu disk}$; $T_{rtt} = 2\pi R_{\mu disk} n_{eff}/c$ is the round trip time inside the micro-disk; $A_{in}^{P/S}$ is the amplitude of the electromagnetic field at the input section of each waveguide; $g^{P/S}$ is a term concerning the rare-earth/light interaction which will be described in the following. Finally, the power out-coupling in the waveguides can be obtained by power conservation.

$\tau_{ext}^{P/S} = 2T_{rtt}/\kappa^2$ is the coupling lifetime related to the coupling between the micro-disk and the waveguide; κ is the cavity decay rate, it is derived by the overlap integral [32]:

$$\kappa = k^2 \frac{n_{\mu disk}^2 - n_{air}^2}{2\gamma_w} \int_{\mathbb{R}^3} \mathbf{E}_w \cdot \mathbf{E}_{\mu disk}^* \, dV \tag{7}$$

where $\mathbf{E}_w$ and $\mathbf{E}_{\mu disk}$ are the electromagnetic field profiles in the waveguides and in the micro-disk, respectively; their power is normalized, i.e. the total power flow through the transversal surface is set equal to 1 W; γ_w is the propagation constant of the waveguide along z direction.

$\tau_0^{P/S} = Q^{P/S}/\omega_{\mu disk}$ is the intrinsic lifetime related to the total power loss. Three different loss phenomena are considered in the model for the evaluation of the quality factor [33]:

$$\frac{1}{Q^{P/S}} = \frac{1}{Q_{abs}^{P/S}} + \frac{1}{Q_{ss}^{P/S}} + \frac{1}{Q_{rad}^{P/S}} \tag{8}$$

$Q_{abs}^{P/S}$ is the quality factor due to the light absorption in the micro-disk and can be expressed as [29]:

$$Q_{abs}^{P/S} = \frac{2\pi n_{eff}}{\zeta \lambda_r} \tag{9}$$

where ζ is a spatially averaged absorption coefficient.

$Q_{ss}^{P/S}$ is the quality factor due to the surface scattering losses. Scattering losses are mainly due to the irregularities on the micro-disk sidewalls. The roughness on the top and the bottom surfaces can be neglected. The scattering quality factor can be expressed as [33]:

$$Q_{ss}^{P/S} = \frac{3\lambda_r^3}{8\pi^{7/2} n_{air}(n_{\mu disk}^2 - n_{air}^2)\vartheta} \frac{V_{\mu disk}}{V_{ss}} \tag{10}$$

where ϑ is the dielectric contrast constant and V_{ss} is the effective volume of a typical scattering structure [33]:

$$\vartheta = \frac{n_{eff}^2(n_{\mu disk}^2 - n_{air}^2)}{n_{\mu disk}^2(n_{eff}^2 - n_{air}^2)}, \; V_{ss} = \sqrt{R_{\mu disk} L_c} h_{\mu disk} \sigma_r \tag{11}$$

n_{eff} is the effective refractive index of the equivalent 1D waveguide, $V_{\mu disk}$ is the volume of the micro-disk, L_c and σ_r are the correlation length and standard deviation of the roughness amplitude, respectively.

$Q_{rad}^{P/S}$ is the quality factor due to the stored internal energy. It is related to the tunneling of light along the curvature of the micro-disk. It can be calculated as in [34]:

$$Q_{rad}^{P/S} = \omega_{\mu disk} \frac{2W_e}{P_d} = \omega_{\mu disk} \frac{2W_m}{P_d} \tag{12}$$

where W_e and W_m are the electric and magnetic energy in the micro-disk, respectively; P_d is the dissipated power.

The signal waveguide is not coupled to disk modes at pump wavelength [35]. Indeed, the signal wavelength is longer than that of the pump. Therefore the distance between the micro-disk and the signal waveguide, if optimized for the signal coupling, is too large to allow the pump out-coupling. Moreover, the pump waveguide is designed in order to be below cut-off at the signal wavelength [35].

Optics EXPRESS

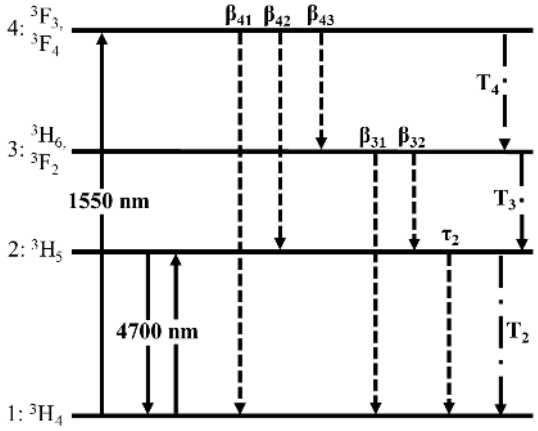

Fig. 2. Four-level model of praseodymium. The most important phenomena are represented: absorption and stimulated emission (full lines), pure-radiative spontaneous decay (dashed lines) and non-radiative spontaneous decay (dash-dotted lines).

2.3. Active behavior model

The four-level model of praseodymium, reported in Fig. 2, is implemented in the computer code in order to simulate the light amplification.

The most important phenomena of rare-earth/light interaction are taken into account in the rate equations:

$$\begin{aligned} N_1 + N_2 + N_3 + N_4 &= N \\ \frac{\mathrm{d}N_4}{\mathrm{d}t} &= \sigma_\mathrm{P} F_\mathrm{P} N_1 - N_4 \left(\frac{1}{T_4} + \frac{\beta_{43}}{\tau_4} + \frac{\beta_{42}}{\tau_4} + \frac{\beta_{41}}{\tau_4} \right) = 0 \\ \frac{\mathrm{d}N_3}{\mathrm{d}t} &= N_4 \left(\frac{1}{T_4} + \frac{\beta_{43}}{\tau_4} \right) - N_3 \left(\frac{1}{T_3} + \frac{\beta_{32}}{\tau_3} + \frac{\beta_{31}}{\tau_3} \right) = 0 \\ \frac{\mathrm{d}N_2}{\mathrm{d}t} &= \sigma_{12} F_{12} N_1 + N_4 \frac{\beta_{42}}{\tau_4} + N_3 \left(\frac{1}{T_3} + \frac{\beta_{32}}{\tau_3} \right) - N_2 \left(\frac{1}{T_2} + \frac{1}{\tau_2} + \sigma_{21} F_{21} \right) = 0 \\ \frac{\mathrm{d}N_1}{\mathrm{d}t} &= -(\sigma_\mathrm{P} F_\mathrm{P} + \sigma_{12} F_{12}) N_1 + N_4 \frac{\beta_{41}}{\tau_4} + N_3 \frac{\beta_{31}}{\tau_3} + N_2 \left(\frac{1}{T_2} + \frac{1}{\tau_2} + \sigma_{21} F_{21} \right) = 0 \end{aligned} \tag{13}$$

where N_i, $i = 1, 2, 3, 4$ is the ion concentration of i-th level; σ_P is the absorption cross section at pump wavelength $\lambda_\mathrm{p} = 1550\,\mathrm{nm}$; σ_{12} and σ_{21} are the absorption and emission cross sections close to signal wavelength $\lambda_\mathrm{s} = 4700\,\mathrm{nm}$, respectively; β_{ij} is the branching ratio from level i to level j; τ_i and T_i are the ion lifetimes for pure-radiative and non-radiative transitions from level i, respectively; F_P and F_{21} are the photon flux at pump and signal wavelengths, respectively. In the simulation, the maximum Pr^{3+} concentration $C_\mathrm{Pr} = 10\,000\,\mathrm{ppm}$ is considered. In fact, preliminary targets with this concentration were obtained via cathodic RF magnetron sputtering without particular difficulties. The normalized photoluminescence intensity versus the emission wavelength was recorded for 2S2G:Pr^{3+} samples fabricated on a) SiO_2 confinement layer and on b) selenide confinement layer. By increasing the excitation density, the guided photoluminescence intensity of the transitions coming from the upper manifolds ($^3F_3$,$^3F_4$) increases if compared to the photoluminescence intensity coming from ($^3H_6$,$^3F_2$). This effect could be attributed to cross-relaxation and partly to the reabsorption of the emitted light by excited ions. The model for high concentrations could be completed by including other phenomena such as cross-relaxation and up-conversion after a suitable characterization. However, these transition should slightly

affect the emission around $\lambda_s = 4.7\,\mu m$.

The term concerning the light-matter interaction used in Eq. (6) is written in Eq. (14) for Pr^{3+}-doped glass:

$$g^P = -\frac{c}{n_{eff}} N_1 \sigma_P \Gamma^P,\ g^S = \frac{c}{n_{eff}} (N_2 \sigma_{21} \Gamma^S - N_1 \sigma_{12} \Gamma^S) \tag{14}$$

where $\Gamma^{P/S}$ is the overlap factor of each WGM with the rare-earth profile:

$$\Gamma^{P/S} = \int_{\Omega_d} |E^{P/S}(x, y)|^2 dx dy \tag{15}$$

$E^{P/S}$ is the normalized electric field distribution in the cross sectional plane x-y (Fig. 1) and Ω_d is the doped area on the x-y plane.

In Eq. (6), a term taking into account the equivalent input noise corresponding to one photon, at the signal wavelength and in the bandwidth $\Delta\nu$, is added [25]:

$$A_0 = c N_2 \sigma_{21} \Gamma^S \frac{h \Delta\nu}{\lambda_r n_{eff}^2 \varepsilon_0 A^S} \tag{16}$$

This allows to simulate the lasing action. For the amplifier operation, the gain G of the system is expressed as:

$$G = \left| \frac{A_{out}^S}{A_{in}^S} \right|^2 \tag{17}$$

In order to solve the rate equations of the rare earth model, the cross section of the micro-disk is divided into volume cells, as described in [25]. In particular, the region from half the radius to the edge of the micro-disk, is discretized in 54 volume cells. A variable-step variable-order solver based on the numerical differentiation formulas of orders 1 to 5 is employed to integrate Eq. (13) on the micro-disk volume.

The model described in this section is implemented in a more general code, including different rare earths. It has been validated by considering the Er^{3+}-doped micro-disk described in [35]. In particular, the optimal distances between the micro-disk and the pump/signal waveguides and the two waveguide sections have been optimized since their values were not reported. All the other parameters considered in the simulation are those of [35]. The simulated output signal power, for the optimized structure, is in excellent agreement with that reported in [35], with a relative difference of a few percent.

3. Design of the passive structure

Figure 3 illustrates the transversal section of the designed structure. It is constituted by a Pr^{3+}-doped chalcogenide micro-disk coupled to two coplanar ridge waveguides. A waveguide is designed for signal propagation at the wavelength $\lambda_s = 4700\,nm$ and the other one for the pump at wavelength $\lambda_p = 1550\,nm$. The pump power could be provided by an erbium or an ytterbium/erbium co-doped fiber laser.

h_w, $h_{\mu disk}$ and h_{buffer} are the thicknesses of waveguides, micro-disk and buffer, respectively; w_p and w_s are the widths of pump and signal waveguides, respectively; g_p and g_s are the distances between the micro-disk and the pump/signal waveguide, respectively. In the model, the Si substrate is a semi-infinite layer, while the buffer thickness is $h_{buffer} = 5\,\mu m$ in order to prevent interaction between light and Si substrate.

The micro-disk and the two waveguides are made of $Ga_5Ge_{20}Sb_{10}Se_{65}$ selenide glass. The buffer layer is made of $Ga_5Ge_{20}Sb_{10}S_{65}$ sulphide glass. In order to develop a realistic feasibility investigation, the refractive index wavelength dispersions of preliminary glass samples are

Optics EXPRESS

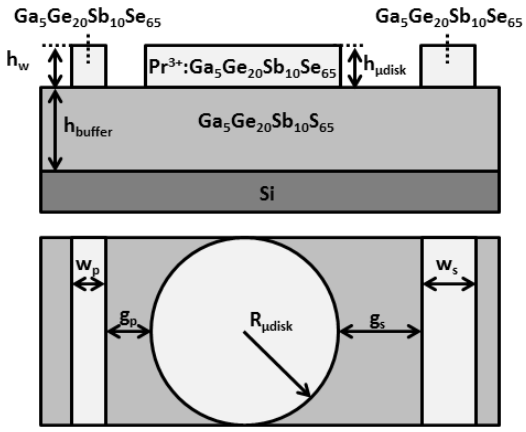

Fig. 3. The praseodymium doped Pr^{3+}:$Ga_5Ge_{20}Sb_{10}Se_{65}$ micro-disk coupled to the two waveguides made of the same glass. A buffer layer of $Ga_5Ge_{20}Sb_{10}S_{65}$ separates the micro-disk from the Si substrate.

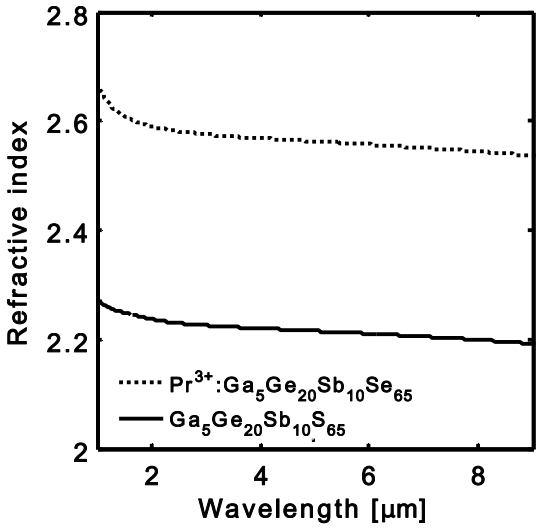

Fig. 4. Measured refractive index as a function of wavelength for Pr^{3+}:$Ga_5Ge_{20}Sb_{10}Se_{65}$, $n_{\mu\text{disk}}$, and $Ga_5Ge_{20}Sb_{10}S_{65}$, n_{buffer}. The measurement is made by NIR and Mid-IR VASE ellipsometry.

Table 1. Refractive indices at signal and pump wavelengths measured by NIR and Mid-IR VASE ellipsometry (±0.001).

Wavelength	Pr^{3+}:$Ga_5Ge_{20}Sb_{10}Se_{65}$	$Ga_5Ge_{20}Sb_{10}S_{65}$
1550 nm	2.607	2.248
4700 nm	2.564	2.217

measured via NIR and Mid-IR VASE ellipsometry [36] and are taken into account in the model. Figure 4 reports the measured refractive index of the buffer n_{buffer} and of the micro-disk $n_{\mu\text{disk}}$ glasses as a function of wavelength. Table 1 reports the refractive indices at signal and pump wavelengths for the two glasses.

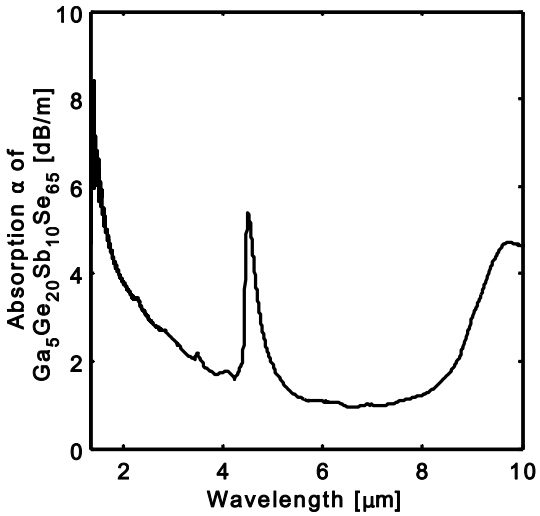

Fig. 5. Absorption coefficient α measured on $Ga_5Ge_{20}Sb_{10}Se_{65}$ un-doped fiber as a function of wavelength.

Table 2. Spectroscopic parameters of the Pr^{3+}:$Ga_5Ge_{20}Sb_{10}Se_{65}$.

Transition	Wavelength [nm]	Branching ratio β	Pure-radiative lifetime τ_i [ms]	Non-radiative lifetime T_i [ms]
$^3H_5 \rightarrow {}^3H_4$	4604	$\beta_{21} = 1.00$	$\tau_2 = 11.36$	$T_2 = 16.70$
$(^3H_6,{}^3F_2) \rightarrow {}^3H_5$	4351	$\beta_{32} = 0.43$	$\tau_3 = 4.66$	$T_3 = 6.09$
$(^3H_6,{}^3F_2) \rightarrow {}^3H_4$	2237	$\beta_{31} = 0.57$		
$(^3F_3,{}^3F_4) \rightarrow (^3H_6,{}^3F_2)$	5769	$\beta_{43} = 0.02$	$\tau_4 = 0.21$	$T_4 = 1.26$
$(^3F_3,{}^3F_4) \rightarrow {}^3H_5$	2481	$\beta_{42} = 0.18$		
$(^3F_3,{}^3F_4) \rightarrow {}^3H_4$	1612	$\beta_{41} = 0.80$		

Figure 5 reports the absorption coefficient α measured on $Ga_5Ge_{20}Sb_{10}Se_{65}$ un-doped glass. The spatially averaged absorption ζ of Eq. (9) is related to the absorption α:

$$\zeta = \alpha \frac{\int_{\Omega_{\mu\text{disk}}} |E^{\text{P/S}}|^2 \, \mathrm{d}x\mathrm{d}y}{\int_{\mathbb{R}^2} |E^{\text{P/S}}|^2 \, \mathrm{d}x\mathrm{d}y} \tag{18}$$

$E^{\text{P/S}}$ is the normalized electric field profile of the considered WGM mode. In the ratio of Eq. (18), the integrals are calculated over the micro-disk cross section (numerator) and over the whole space (denominator).

The quality factor related to the scattering surface losses $Q_{\text{ss}}^{\text{P/S}}$ is calculated by using correlation length $L_c = 150\,\text{nm}$ and standard deviation $\sigma_r = 10\,\text{nm}$ [35]. The quality factor related to the radiation $Q_{\text{rad}}^{\text{P/S}}$ is evaluated by using the electromagnetic field obtained via FEM simulation.

Table 2 reports branching ratios β_{ij}, pure-radiative lifetimes τ_i and non-radiative lifetimes T_i calculated by Judd-Ofelt method for the considered Pr^{3+}-doped $Ga_5Ge_{20}Sb_{10}Se_{65}$ glass with concentration $C_{\text{Pr}} = 1000\,\text{ppm}$. Figure 6 illustrates the absorption and emission cross-sections of the same glass.

At first, the signal waveguide is simulated with FEM solver by changing the width in the range 1 μm–10 μm with a step of 0.5 μm and the thickness in the range 0.5 μm–1.5 μm with a step of 0.1 μm. The confinement factor Ω is evaluated for each waveguide mode as the ratio of

Optics EXPRESS

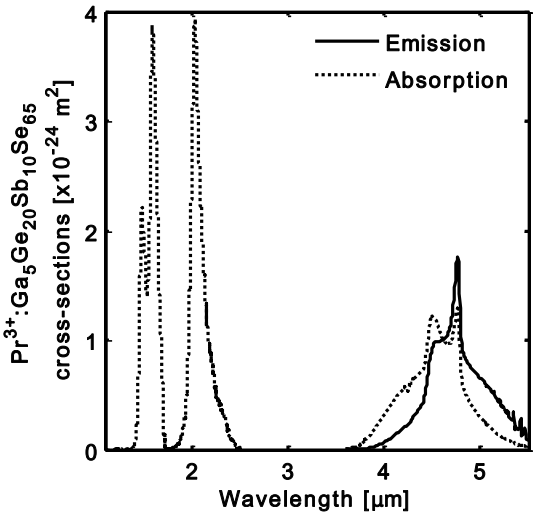

Fig. 6. Calculated emission and absorption cross-sections for the Pr^{3+}:$Ga_5Ge_{20}Sb_{10}Se_{65}$ glass.

the integrals of normalized electric field profile E_w of the considered waveguide mode calculated over the waveguide cross-section and over the whole space:

$$\Omega = \frac{\int_{\Omega_{\mu\text{disk}}} |E_w|^2 \, dx dy}{\int_{\mathbb{R}^2} |E_w|^2 \, dx dy} \tag{19}$$

Figure 7 reports the confinement factor Ω as a function of width and height for a single-mode waveguide. For a fixed height, by increasing the width, the waveguide is at first below the cut-off and then exhibits single-mode propagation, for larger width it exhibits multi-mode propagation. Only single mode propagation is represented. Furthermore, in single-mode case, the confinement factor Ω increases with the waveguide width, i.e. the evanescent field becomes weaker. The pixels have a gray tone which is dark if Ω is low and bright if Ω is large. As an example, Fig. 8 illustrates the electric field norm distribution for single-mode waveguides at signal wavelength having height $h_w = 1\,\mu m$ and width a) $w_s = 3.5\,\mu m$ and b) $w_s = 6.5\,\mu m$. The confinement factors are $\Omega = 0.20$ and $\Omega = 0.34$. It is apparent that a large confinement factor Ω indicates small evanescent tails.

A height $h_w = 1.2\,\mu m$ and a width $w_s = 3.5\,\mu m$ are chosen for the signal waveguide. The micro-disk and the two waveguides have the same thickness, $h_{\mu\text{disk}} = h_w = 1.2\,\mu m$. This choice is made by supposing to exploit an RF sputtering process for the device construction.

The FEM solver is used to simulate the pump waveguide and a width $w_p = 0.5\,\mu m$ is identified in order to obtain a single-mode operation. In the signal waveguide the fundamental mode polarization is quasi-TE, while in the pump waveguide it is quasi-TM.

Figure 9 reports the micro-disk effective refractive index n_{eff} as a function of micro-disk thickness obtained via Eq. (2) for $\lambda_s = 4700\,nm$. In case of $h_{\mu\text{disk}} = 1.2\,\mu m$, the effective refractive index is $n_{\text{eff}} = 2.33$ for the fundamental mode having longitudinal parameter $p = 1$. The characteristic equation Eq. (5) is solved by imposing fundamental WGM solution, i.e. by putting $l = m$ and the further condition $n = 1$. The micro-disk radius $R_{\mu\text{disk}}$ and the azimuthal parameter m of the WGM having resonant wavelength close to $\lambda_s = 4700\,nm$ are identified.

Figure 10 illustrates the micro-disk radius $R_{\mu\text{disk}}$ as a function of wavelength obtained by solving Eq. (5). The smallest admissible micro-disk radius $R_{\mu\text{disk}} = 65\,\mu m$ is chosen. This allows to reduce the computational cost of the simulation.

Optics EXPRESS

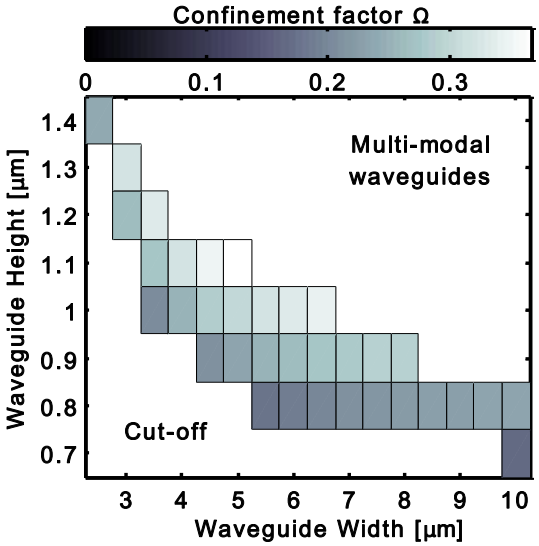

Fig. 7. Confinement factor Ω as a function of width and height for single-mode signal waveguide.

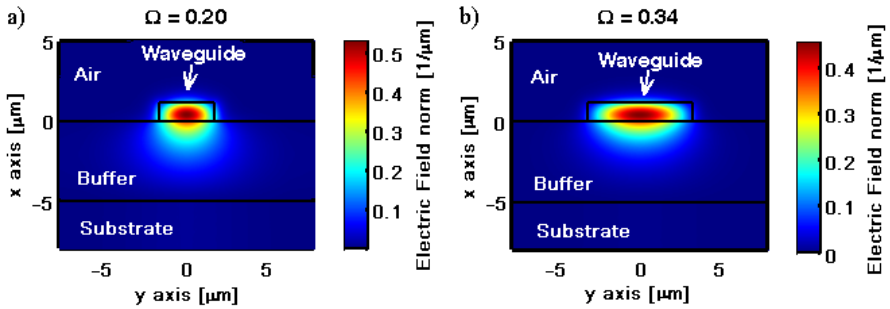

Fig. 8. Distribution of the electric field norm for the fundamental mode in signal waveguide having $h_w = 1\,\mu m$ and a) $w_s = 3.5\,\mu m$, b) $w_s = 6.5\,\mu m$.

The micro-disk obtained using the coarse design method is tested with FEM solver in order to verify the resonance at signal and pump wavelengths and find more accurate solutions.

To resume the passive design, the suitable geometrical parameters of the micro-disk and the coupling waveguides are chosen by considering i) a suitable micro-disk radius in order to have resonance at both the pump and signal wavelengths; ii) waveguide dimensions in order to have single-mode propagation resonance at both the pump and signal wavelengths and maximize the overlapping factor Ω; iii) the same thickness for waveguides and micro-disk because of sputtering process; iv) buffer thickness in order to prevent interaction between waveguide and Si substrate. The optimized geometrical parameters are listed in Table 3.

Figure 11 illustrates the distribution of the electric field norm for the fundamental signal mode $WGM_{194,1,1}$ and the fundamental waveguide mode with $g_s = 4.3\,\mu m$ for the passive device.

4. Active structure design

The FEM solver is used to simulate the micro-disk WGMs and the waveguide propagation modes by considering the geometrical parameters of Table 3. In the simulations, the fundamental mode $WGM_{194,1,1}$ at the signal wavelength $\lambda_s = 4700\,nm$ is considered. Moreover, the first seven

Optics EXPRESS

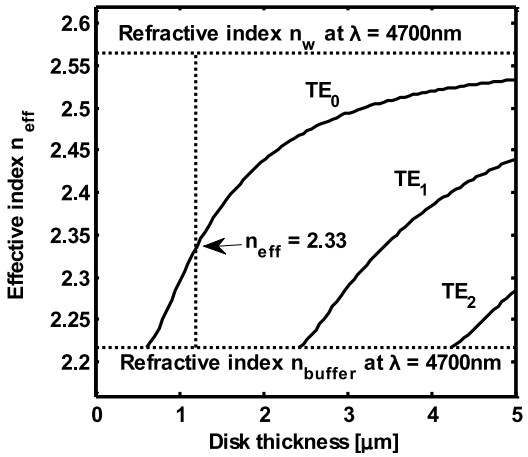

Fig. 9. Micro-disk effective refractive index n_{eff} as a function of disk thickness for $\lambda_{\mathrm{s}} = 4700\,\mathrm{nm}$. The subscript p in $\mathrm{TE_p}$ is the longitudinal parameter of the considered $\mathrm{WGM_{m,n,p}}$.

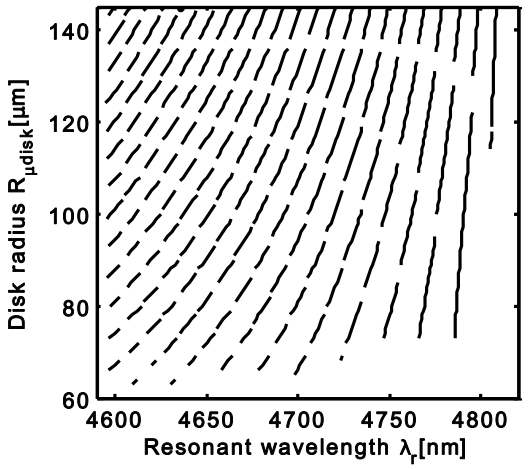

Fig. 10. Micro-disk radius $R_{\mu\mathrm{disk}}$ as a function of the resonant wavelength obtained by solving Eq. (5).

Table 3. Geometry of the optimized amplifier.

Dimension	Value [μm]
Micro-disk radius $R_{\mu\mathrm{disk}}$	65.0
Micro-disk and waveguides thicknesses $h_{\mu\mathrm{disk}} = h_{\mathrm{w}}$	1.2
Buffer thickness h_{buffer}	5.0
Signal waveguide width w_{s}	3.5
Pump waveguide width w_{p}	0.5

WGMs are considered at the pump wavelength $\lambda_{\mathrm{p}} = 1550\,\mathrm{nm}$. The signal gain is maximized by exploiting different pump modes in order to increase the interaction between pump and rare earth, in order to generate/amplify the signal [35]. Table 4 reports the parameters of the simulated modes.

The output signal power $P_{\mathrm{out}}^{\mathrm{signal}}$ versus the distance g_{p} between micro-disk and pump waveguide

Optics EXPRESS

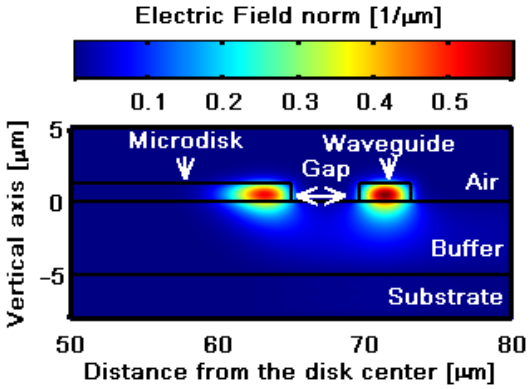

Fig. 11. Distribution of the electric field norm for the fundamental signal mode $WGM_{194,1,1}$ and the fundamental waveguide mode with $g_s = 4.3\,\mu m$.

Table 4. WGM characteristics at signal and pump wavelengths.

$WGM_{m,n,p}$	λ_r [nm]	$Q_{abs} \times 10^6$	$Q_{ss} \times 10^4$	$Q_{rad} \times 10^7$	$Q \times 10^4$
Signal mode					
$WGM_{194,1,1}$	4669.0	5.58	132.71	1.48	99.96
Pump modes					
$WGM_{657,1,1}$	1550.4	7.71	4.90	96.4	4.87
$WGM_{645,2,1}$	1550.0	7.57	4.86	96.1	4.83
$WGM_{635,3,1}$	1550.2	7.45	4.83	95.7	4.79
$WGM_{626,4,1}$	1550.7	7.35	4.81	95.1	4.77
$WGM_{618,5,1}$	1550.7	7.26	4.78	93.7	4.51
$WGM_{611,6,1}$	1549.7	7.18	4.74	91.3	4.71
$WGM_{604,7,1}$	1549.6	7.10	4.72	90.8	4.69

is simulated for the input signal power $P_{in}^{signal} = -30\,dBm$ and input pump power $P_{in}^{pump} = 100\,mW$, praseodymium concentration $C_{Pr} = 3000\,ppm$ and distance between micro-disk and signal waveguide $g_s = 4.45\,\mu m$. By increasing the distance g_p between micro-disk and pump waveguide, an almost constant and maximized signal power P_{out}^{signal} is simulated till $g_p = 350\,nm$. Then, for larger g_p values, the output signal power P_{out}^{signal} decreases. A value $g_p = 200\,nm$ is chosen.

Figure 12 depicts the maximum output signal power $P_{out,MAX}^{signal}$ as a function of input pump power P_{in}^{pump} and praseodymium concentration C_{Pr}. The simulations are performed by changing the input pump power P_{in}^{pump} in the range 0.01 mW–50 mW, the distance g_s between micro-disk and signal waveguide in the range 0.5 μm–5.5 μm and the praseodymium concentration C_{Pr} in the range 100 ppm–10 000 ppm. The input signal power is $P_{in}^{signal} = -30\,dBm$. The maximum output signal power $P_{out,MAX}^{signal}$ is the largest value obtained within the g_s range. By increasing the input pump power P_{in}^{pump} or praseodymium concentration C_{Pr}, the maximum output signal power $P_{out,MAX}^{signal}$ increases. The increase of P_{in}^{pump} or C_{Pr} yields a similar effect. The population inversion is improved and thus the output signal power P_{out}^{signal} is maximized.

Figure 13 illustrates the optical gain G, as defined in Eq. (17), as a function of distance g_s between micro-disk and signal waveguide for the input pump power $P_{in}^{pump} = 0.01\,mW$. It is

Optics EXPRESS

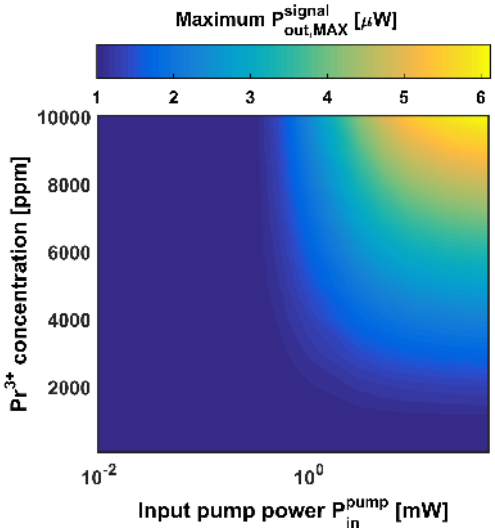

Fig. 12. Maximum output signal power $P^{\text{signal}}_{\text{out,MAX}}$ as a function of input pump power $P^{\text{pump}}_{\text{in}}$ and praseodymium concentration C_{Pr}. The input pump power $P^{\text{pump}}_{\text{in}}$ varies in the range 0.01 mW–50 mW and the praseodymium concentration C_{Pr} in the range 100 ppm–10 000 ppm. The input signal power is $P^{\text{signal}}_{\text{in}} = -30$ dBm.

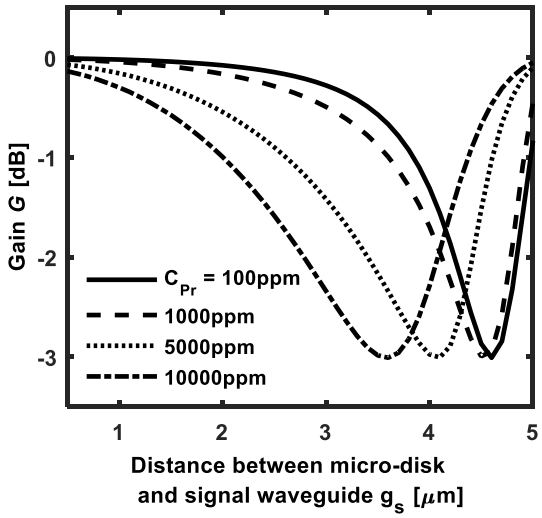

Fig. 13. Optical gain G as a function of distance g_{s} between micro-disk and signal waveguide for different praseodymium concentrations. The input pump power is $P^{\text{pump}}_{\text{in}} = 0.01$ mW and the input signal power is $P^{\text{signal}}_{\text{in}} = -30$ dBm.

apparent that the input pump power is too weak to achieve the inversion of population. The optical gain is negative because the losses due to the light propagation in the micro-disk are predominant with respect to the gain.

Figure 14 illustrates the optical gain G as a function of distance g_{s} between micro-disk and signal waveguide for the input pump power $P^{\text{pump}}_{\text{in}} = 50$ mW. For $C_{\text{Pr}} = 100$ ppm and $C_{\text{Pr}} = 1000$ ppm, the concentration is too low to have optical gain. By increasing the praseodymium

Optics EXPRESS

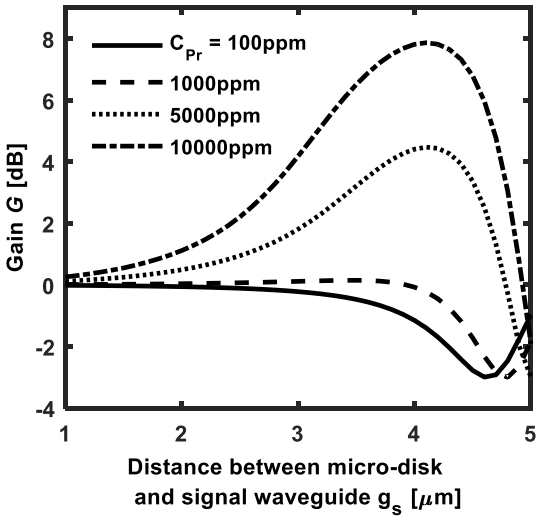

Fig. 14. Optical gain G as a function of distance g_s between micro-disk and signal waveguide for different praseodymium concentrations. The input pump power is $P_{in}^{pump} = 50\,mW$ and the input signal power is $P_{in}^{signal} = -30\,dBm$.

concentration C_{Pr}, the input pump power activates the interaction between light and rare earth. The maximum gain is $G \approx 7.9\,dB$ and it is obtained with $C_{Pr} = 10\,000\,ppm$ and $g_s \approx 4.1\,\mu m$. By increasing the concentration, the peak of the optical gain G is obtained for smaller values of the distance g_s between micro-disk and signal waveguide. In fact, by increasing the ions populations, the signal absorption increases due to the transition $^3H_4 \rightarrow {}^3H_5$. In order to compensate this larger absorption, a stronger optical coupling is needed.

Figure 15 reports the ions populations as a function of the time t in the case of the highest gain $G \approx 7.9\,dB$, obtained for $P_{in}^{pump} = 50\,mW$, $C_{Pr} = 10\,000\,ppm$ and $g_s = 4.1\,\mu m$. At the initial time $t = 0\,s$, the pump signal is applied. The pump absorption at the wavelength $\lambda_p \approx 1.55\,\mu m$ yields a fast decrease of the population N_1 of the ground level $^3H_4$ and an increase of the population N_4 of the level ($^3F_3$,$^3F_4$). Afterwards, the spontaneous decays (radiative and non-radiative) lead to an increase of the populations N_3 and N_2 of levels ($^3H_6$,$^3F_2$) and $^3H_5$, respectively. The light emission at $\lambda_s \approx 4.7\,\mu m$ is related to the transition $^3H_5 \rightarrow {}^3H_4$ (ions populations N_2 and N_1).

Figure 16 illustrates the laser characteristic, i.e. the output signal power P_{out}^{signal} as a function of the input pump power P_{in}^{pump}, with $C_{Pr} = 10\,000\,ppm$. In the laser behavior, the maximum value of output signal power P_{out}^{signal} is obtained with $g_s \approx 4.1\,\mu m$. The pump threshold is close to 0.4 mW. The slope efficiency S is defined as the ratio between the output signal power and the input pump power. The best slope efficiency is close to $S = 8.1 \times 10^{-4}$ in the range of input pump power from 2 mW to 6 mW. This value is about six times higher than that simulated for an optimized erbium-doped micro-disk, emitting at 4.5 μm, via the same home-made computer code, according to the results reported in [35].

5. Conclusion

For the first time to the best of our knowledge, the design of an amplifier based on a chalcogenide Pr^{3+}-doped micro-disk coupled to two ridge waveguides is performed. A home-made computer code is developed to this aim. The micro-disk has a radius of 65 μm and a thickness of 1.2 μm. A very high gain $G \approx 7.9\,dB$ is simulated for a Pr^{3+} concentration of 10 000 ppm, an input signal power of −30 dBm at the wavelength 4.7 μm and an input pump power of 50 mW at the

Optics EXPRESS

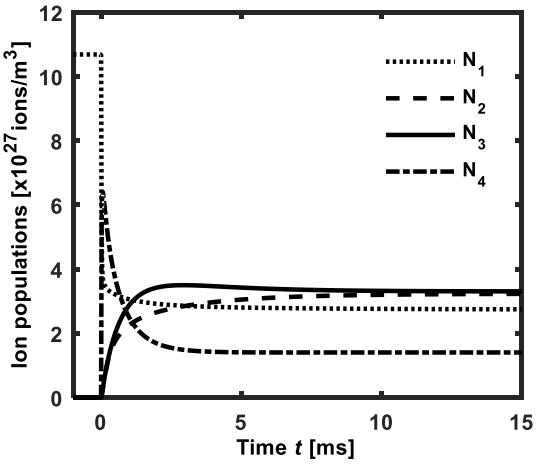

Fig. 15. Ions populations as a function of the time in the case of the highest gain: $P_{\text{in}}^{\text{pump}} = 50\,\text{mW}$, $P_{\text{in}}^{\text{signal}} = -30\,\text{dBm}$, $C_{\text{Pr}} = 10\,000\,\text{ppm}$, $g_{\text{s}} = 4.1\,\mu\text{m}$. In $t = 0\,\text{s}$ the pump signal is applied.

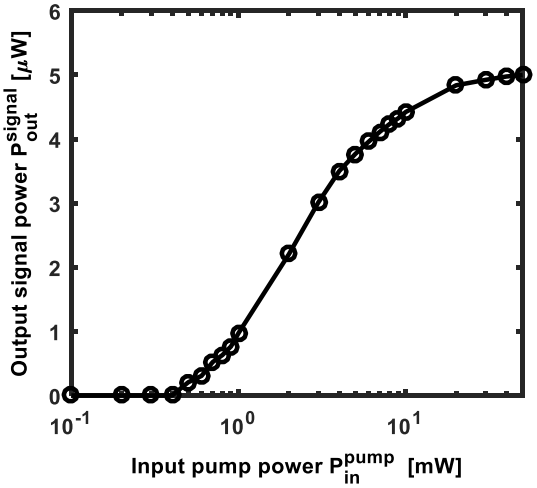

Fig. 16. Output signal power $P_{\text{out}}^{\text{signal}}$ as a function of the input pump power $P_{\text{in}}^{\text{pump}}$ with $C_{\text{Pr}} = 10\,000\,\text{ppm}$ and $g_{\text{s}} = 4.3\,\mu\text{m}$.

wavelength 1.55 μm. In the laser behavior, the maximum slope efficiency $S = 8.1 \times 10^{-4}$ is obtained for Pr^{3+} concentration of 10 000 ppm and input pump power in the range 2 mW–6 mW. The pump threshold is 0.4 mW.

Funding

This research was performed within MIUR plans: PON01 01224 “Sviluppo di tecnologie in guida d’onda integrata (SIW) per applicazioni ICT a microonde”; PONa3 00298 “Potenziamento delle strutture e delle dotazioni scientifiche e tecnologiche del polo scientifico e tecnologico Magna Grecia”; PON02 00576 3329762 “Sistemi avanzati mini-invasivi di diagnosi e radioterapia” AMIDERHA; COST Action MP1401 Advanced Fibre Laser and Coherent Source as tools for Society, Manufacturing and Lifescience.